Direct Imaging of Heteroatom Dopants in Catalytic Carbon Nano-Onions

Journal:	*Nanoscale*
Manuscript ID	NR-ART-01-2020-000335.R1
Article Type:	Paper
Date Submitted by the Author:	24-Feb-2020
Complete List of Authors:	Thomas, Melonie P.; University of Kentucky Wanninayake, Namal; University of Kentucky De Alwis Goonatilleke, Manisha; University of Kentucky Kim, Doo Young; University of Kentucky Guiton, Beth; University of Kentucky

SCHOLARONE™
Manuscripts

ARTICLE

Direct Imaging of Heteroatom Dopants in Catalytic Carbon Nano-Onions

Melonie P. Thomas,[#a] Namal Wanninayake,[#a] Manisha De Alwis Goonatilleke[a], Doo Young Kim,*[a] and Beth S. Guiton*[a]

The hollow core, concentric graphitic shells, and large surface area of the carbon nano-onion (CNO) make these carbon nanostructures promising materials for highly efficient catalytic reactions. Doping CNOs with heteroatoms is an effective method of changing their physical and chemical properties. In these cases, the configurations and locations of the incorporated dopant atoms must be a key factor dictating catalytic activity, yet determining a structural arrangement on the single-atom length scale is challenging. Here we present direct imaging of individual nitrogen and sulfur dopant atoms in CNOs, using an aberration-corrected scanning transmission electron microscopy (STEM) approach, combined with electron energy loss spectroscopy (EELS). Inspection of the statistics of dopant configuration and location in sulfur-, nitrogen-, and co-doped samples reveals dopant atoms to be more closely situated to defects in the graphitic shells for co-doped samples, than in their singly doped counterparts. Correlated with an increased activity for the oxygen reduction reaction in the co-doped samples, this suggests a concerted mechanism involving both the dopant and defect.

a. Department of Chemistry, University of Kentucky, Lexington, Kentucky 40506, United States

†
#these two authors contributed equally.
*Corresponding authors: beth.guiton@uky.edu, dooyoung.kim@uky.edu
ORCID:
Melonie P. Thomas: 0000-0002-5264-1921
Namal Wanninayake: 0000-0002-8875-8726
Manisha De Alwis Goonatilleke: 0000-0002-9013-9086
Doo Young Kim: : 0000-0002-6095-5023
Beth S. Guiton: 0000-0002-9478-9190

Introduction

Carbon-based nanomaterials where heteroatoms or metal-ligand complexes are embedded have been investigated as an effective alternative to replace precious Pt-based catalysts, mainly due to their cost effectiveness, long-term stability and comparable catalytic activity.[1–7] Carbon nano-onions (CNOs) are multi-shelled carbon nanostructures with a hollow core and concentric polyhedral shells, which can be synthesized by thermal annealing of nano-diamonds, chemical vapor deposition, arc-discharge, etc.[8–11] CNOs exhibit high electrical conductivity and chemical activity due to high surface curvature and strain energy. Due to a high specific-surface-area and catalytic surface, CNOs are useful for chemical and electrochemical conversions.[12] With the presence of many active sites due to the large surface area and significant number of defects, CNOs have shown high efficiencies to catalyze reactions such as C-H bond activation, oxygen reduction reaction (ORR), ring opening polymerization, alcohol oxidation, and styrene epoxidation.[2,8,13–15]

Doping CNOs with non-metallic heteroatoms is known to be an effective method to change their physical and chemical properties.[2] Compared to undoped CNOs, N- and B-doped CNOs have shown enhanced catalytic activity in styrene epoxidation reactions and the ORR.[2,8] Lin et al. reported that N heteroatom dopants produce a large number of structural defects in the graphitic shells of the CNO, which can explain its enhanced catalytic activity in styrene epoxidation reactions.[8] Moreover, it has been shown that CNOs with higher number of defect sites are more susceptible to reactions occurring at the surface.[16] The configurations and locations of the dopant atoms and defects, therefore, are likely key factors determining the catalytic activity of heteroatom doped CNOs.[17] Recent studies of doped catalytic CNOs have shown the structure of concentric graphitic layers of the CNO via TEM/STEM.[2,8,9,11,18] Previous computation studies have identified specific chemical configurations involving single dopant or multiple dopants in close proximity to one another as candidates for efficient catalysis.[14] Nonetheless, experimental evidence that confirms such sites have been rarely reported. A detailed structural analysis is imperative, therefore, to locate heteroatom dopants and associated defects. As an example, to further understand the effect of co-heteroatom-doped carbon host structures towards

catalytic mechanisms such as the oxygen reduction reaction (ORR) or electrochemical carbon dioxide reduction,[19] atomic-scale visualization of the catalyst is crucial. The structural details provided by such analysis can be used directly for building computational models for which density functional theory (DFT) calculations are utilized to deduce viable reaction pathways for these mechanisms.[20]

Motivated by aforementioned necessities, here, we report the direct imaging of heteroatoms in doped CNOs for the first time, via aberration-corrected STEM equipped with EELS, and provide an analysis of dopant configuration and location with respect to discontinuity/defect sites in the CNO graphitic shells, for three CNO samples: sulfur-doped CNOs (S-CNO), nitrogen-doped CNOs (N-CNO), and nitrogen and sulfur co-doped CNOs (NS-CNO). Finally, ORR catalytic activities of these samples were compared to gain more insights on the role of heteroatom dopants on CNOs and enhanced catalytic activity of NS-CNO with respect to N- and S-CNO.

Experimental

Synthesis of CNOs, S-, N-, and, SN-CNO:

Synthesis of CNOs: CNOs were prepared by thermally annealing nanodiamond powder ~5 nm (Dynalene NB50, purchased from Nanostructured & Amorphous Materials, Inc.) at 1700 °C for 1 hour under the flow of Helium using a graphitization furnace. Then, the CNOs were further annealed using the same furnace under air at 400 °C for 4 hours to remove any adventitious impurities.

Synthesis of Ox-CNO (oxidized carbon nano onions): First, 500 mg of previously prepared CNOs were mixed with 36 ml of concentrated HNO3 (Fisher Scientific, Assay-69.5%) and 64 ml of deionized (DI) water (18.2 MΩ) in a 100 ml three neck flask. Then, the solution was subjected to ultrasonic agitation for 15 minutes to form a homogeneous solution. Next, a magnetic stir bar was added, and the solution was refluxed at 105 °C for 4 hours under 400 rpm. After cooling down, the solution was centrifuged and washed with DI water several times until the solution pH becomes neutral. Finally, the product was vacuum dried at 60 °C to obtain Ox-CNO.

Synthesis of N-CNO: First, 200 mg of Ox-CNO and 1 g of urea (Sigma Aldrich, ACS reagent, 99.0-100.5%) were added into a 10 ml methanol solution (Sigma Aldrich, anhydrous, 99.8%). Then the solution was ultrasonically agitated for 10 minutes. After that, the

methanol was slowly evaporated, and the resulting solid was crushed into a powder using a mortar and pestle. Subsequently, the solid was placed in a quartz boat and placed inside of a tubular furnace (LINDBERG/BLUE M, Mini-Mite Tube Furnace). The tube was then heated to 700 °C for 3 hours under argon protected environment (Scott-Gross, 99.999%) with a heating ramp rate of 5 °C min^{-1}. Resulting solid was washed with DI water several times to remove any soluble byproducts. Finally, N-CNO were isolated by removing the water at 60 °C in a vacuum oven.

Synthesis of S-CNO: First, 60 mg of Ox-CNO, 18 ml of dimethyl sulfoxide (Sigma Aldrich, 99.9%), and 2 ml of DI water were added into a Teflon lined container. Then, the Teflon container was closed and ultrasonically agitated for several minutes before placing inside of a stainless-steel autoclave. After that, the autoclave reactor was heated to 180 °C for 18 hours in an oven. The resulting solid was washed with ethanol (Sigma Aldrich, Reagent Alcohol 95%) and DI water several times. The solid was then dried by removing the solvents at 60 °C under vacuum and placed in a tubular furnace. Finally, the tube was heated at 700 °C for 1 hr under 5% hydrogen in argon to obtain S-CNO.

Synthesis of NS-CNO: NS-CNO were prepared following the same procedure used to synthesize N-CNO. In this synthesis, instead of urea, thiourea (Sigma Aldrich, ≥99.999% (metals basis)) was used as the nitrogen and sulfur donor.

STEM sample preparation

A small amount of the as-synthesized powder sample was dispersed in high purity isopropanol (Sigma-Aldrich) and sonicated for 30 minutes. 10 µL of the diluted solution mixture was drop-cast onto a 300 mesh Cu grid with a holey carbon film. The drop-cast grids were annealed at 80 °C for 8 hours in vacuum prior to the STEM characterization.

STEM characterization

STEM characterization was performed using in Nion UltraSTEM 100 (U100) at 100 kV with a probe current of 0.5 nA (atomic-size probe). The Nion U100 is equipped with 5th-order Nion aberration-corrector and Gatan Enfina EELS which can achieve energy resolutions <350 meV at 100 kV. The Hartree-Slater model was used in obtaining the energy differential cross-section in EELS spectra. After the EELS spectrum is obtained, a background correction operation was performed to improve the signal to noise ratio.

Filtering

Filtering was performed to eliminate noise from high resolution micrographs while retaining the information from CNO lattice fringes and dopant atoms. For a particular HAADF micrograph obtained, a fast Fourier transform (FFT) was acquired using Gatan Digital Micrograph® software. In the FFT, rings corresponding to the interlayer spacings of the CNOs in were masked, and an inverse FFT (IFFT) operation was performed to regenerate the parts of the image containing selected masked frequencies.

Catalytic activity determination

Electrode preparation

First, 8 mg of the catalyst, 250 µL ethanol (Sigma Aldrich, anhydrous, ≥99.5%), 750 µL Isopropyl alcohol (BDH, VWR analytical, assay 99.5%), and 60 µL Nafion (Sigma Aldrich, 117 solution ~5 wt%) were mixed and sonicated for 30 minutes to form a homogeneous catalyst ink solution. Then, a rotating ring disk electrode (RRDE) unit equipped with a glassy carbon disk (4 mm diameter) and Pt ring, was polished with alumina powder. After that, 8.4 µL of the prepared catalyst ink was drop casted on to the glassy carbon disk and dried at 60 °C overnight. As a comparison, commercial Pt-C catalyst (20% (w/w) Pt, Vulcan XC-72, Premetek Co) on glassy carbon was also prepared using the same method.

ORR activity measurements

ORR activity of each catalyst was determined via rotational ring-disk electrode (RRDE) measurements in a 0.1 M KOH electrolyte solution (Fluka analytical). First, the electrolyte solution was saturated with oxygen (Scott-Gross, 99.99%) by purging the gas for 30 minutes. A platinum (Pt) coil was used for the counted electrode (CE). The catalyst or Pt/C mounted disk electrode was used for the first working electrode (WE). The Pt ring electrode was connected to the second working electrode where fixed potential is applied. A Ag/AgCl electrode (CH Instruments) filled with 1M KCl was used as the reference electrode (RE). Linear sweep voltammograms (LSV) were recorded under the rotation rate of 1600 rpm while the disk potential was swept from 0.25 to -0.85 V vs. Ag/AgCl at the scan rate of 5 mVs^{-1} and the Pt-ring potential is fixed at 0.30 V vs. Ag/AgCl to oxidize back hydrogen peroxide. The electron transfer number (n) was then determined by the following equation.

$$n = \frac{4 \cdot I_d}{I_d + \left(\frac{I_r}{N}\right)}$$

Where I_d is the disk current, I_r is the ring current, N is the collection efficiency of the Pt-ring. N was determined to be 0.42 from the RRDE experiment with $K_4Fe(CN)_6$.

Raman spectroscopy measurements

Raman spectroscopic measurements were obtained with a DXR micro-Raman instrument (Thermo Scientific). Each Raman spectra was collected (32 scans, 5 mW power with 3 second sample exposure time) using a diode-pumped 532 nm Nd:YVO$_4$ laser as the excitation source.

X-ray photoelectron spectroscopy (XPS) measurements

A Thermo Scientific K-Alpha photoelectron spectrometer was used to probe the elemental compositions of the samples. Powder samples were mounted on the powder sample holder. XPS measurements were conducted by focusing monochromatic Al K-α radiation (energy of 1486.6 eV) onto 400 μm diameter spot on the sample. During the measurement, a flood gun is used to minimize sample charging.

images (second column) of N-, S-, and, NS-CNO samples. In the third column, the heteroatom dopants (green) and graphitic shells of CNO (red) are false colored to enable recognition of dopant atoms. Images reveal that the onion like concentric shell structure of the CNO has been retained during the doping step. The interlayer spacing of the graphitic shells of N-, S-, and, NS-CNO are ~0.33 nm, consistent with the 0.33-0.35 nm range in previous reports.[21,22] The heteroatom dopants (N and S) and their configuration (whether they are arranged in groups or as single atoms (Fig. S1)) can be seen clearly in the HRSTEM images. High-angle annular dark field (HAADF), also known as Z-contrast imaging mode, is a STEM imaging mode using an annular detector to collect electrons scattered through high angles (usually >80 mrad)[23]. The scattering intensity of electrons on this detector is roughly proportional to $Z^{1.6-1.9}$,[24] and this mode therefore produces an image in which higher mass atoms and materials correspond to regions of higher intensity, and images which are easily interpretable. The contrast observed in Fig. 1 (first column) therefore represents
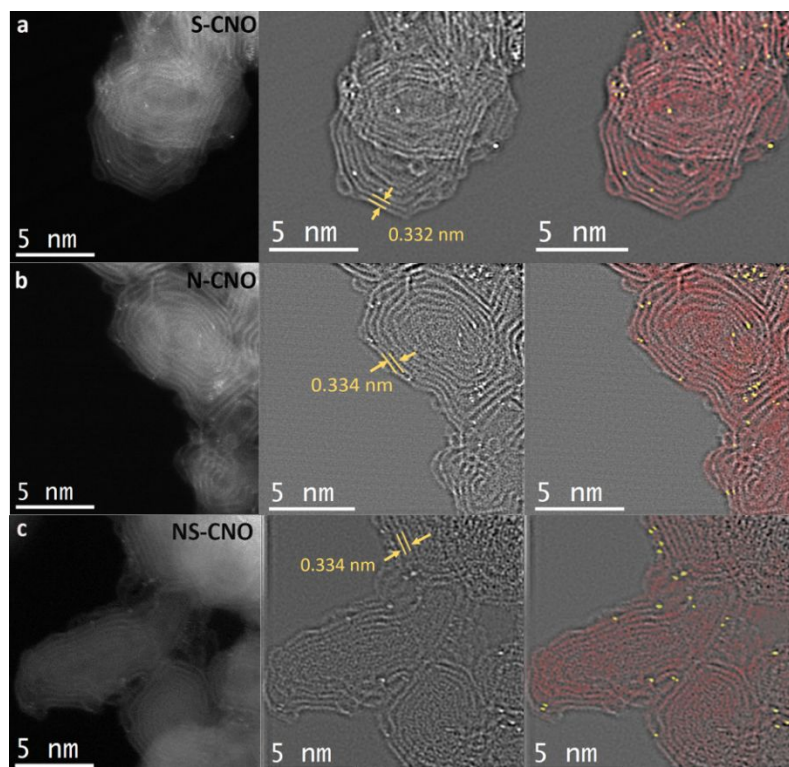
Figure 1. HRSTEM images of CNO with heteroatom dopants, (a) sulfur-doped, (b) nitrogen-doped, and (c) sulfur and nitrogen co-doped, and their respective IFFT filtered (middle) and false-colored (right column) images. Red=carbon; yellow=dopant atom.

Results and discussion

Figure 1 shows high resolution STEM (HRSTEM) micrographs (first column) and their respective filtered

concentric spherical shells, with individual and grouped dopant atoms of higher atomic number than the shell. Individual atoms identified through their high intensity in the HAADF image have been false colored (column 3) for clarity.
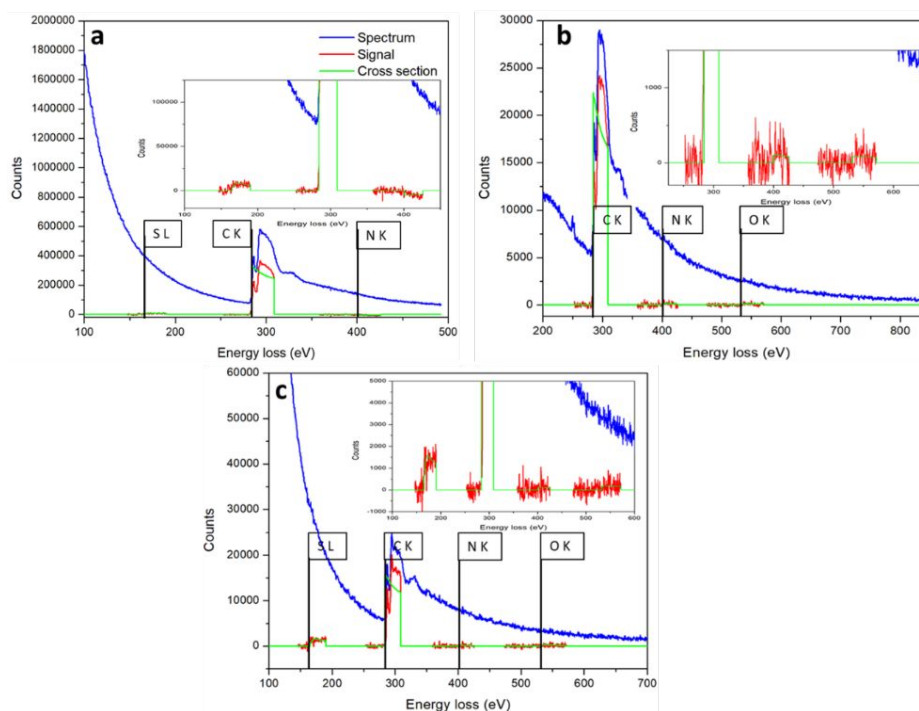
Figure 2. EEL spectroscopy. (a) Sulfur-doped, (b) nitrogen-doped, and (c) sulfur and nitrogen co-doped, CNO samples, confirming successful doping of the respective heteroatoms into the CNO structure

EEL spectroscopy (Fig. 2) performed on all three samples confirms the presence of carbon, nitrogen, and sulfur as expected. An oxygen signal was also recorded, and can be attributed to oxygenated functional groups formed during chemical oxidation of CNOs prior to doping process. The oxygen signal was found in all three samples. The EELS edges of N and S can be identified clearly, and are shown in the magnified regions of the spectra inset Fig. 2. Defects such as discontinuities and holes in graphitic shells of CNO (Fig. S2) are identified with red arrows in filtered micrographs of the three doped samples (Fig. 3).

While EELS analysis provides information regarding the chemical composition in the local structure, X-ray photoelectron spectroscopy (XPS) measurements can be used to determine the overall surface elemental compositions. Figure S3 and Table S4 indicate XPS survey spectra and a summary of elemental compositions. The survey scan of each sample indicates that the prepared samples are free of other impurities and contain only C, N, S and O further confirming the successful incorporation of heteroatoms. All heteroatom-doped samples showed about 2 at. % of S and/or N. The content of oxygen in ox-CNO is high due to the formation of oxygen functional groups and subsequent heteroatom doping reduces the oxygen

content (to about 1 at. % or less) in exchange for heteroatoms.

Raman spectroscopy was utilized to understand the microstructure and defects in these carbon materials. As shown in Figure S4, Raman spectra of all samples contain three peaks centered at ~1335 cm^{-1}, ~ 1570 cm^{-1} and ~2663 cm^{-1} corresponding to D- band, G-band and 2D-band, respectively. The intensity ratio, I_D/I_G (the ratio between the intensities of D- band and G- band in Raman spectra) is a measurement of the material disorder.[25] The calculated I_D/I_G ratios for CNO, Ox-CNO, N-CNO, S-CNO and NS-CNO are 0.95, 1.16, 1.24, 1.18 and 1.41, respectively (Fig. S4). These results indicate that CNO has the lowest disorder and NS-CNO has the highest disorder due to the contribution from both N and S atoms.

The defects form edges in concentric graphene shells and play an important role in catalysis. STEM imaging indicates that the proximity of the dopant to the defect is important and we might gain insight from a quantitative analysis of the configuration of the heteroatom dopants (whether they are present as isolated atoms, or as groups), and their proximity to defects within the graphitic shells. Data taken from the three samples is summarized in Table 1 (detailed information is available in Table S1-3). This represents

measurement of 98 CNOs, 358 dopant atoms/groups, and 358 defects in total. It should be noted that the STEM micrograph is a two-dimensional (2D) projection of a three-dimensional (3D) sample, and as such only the defects which are visible in 2D micrographs were

considered, therefore. It is worth noting, however, that since we are using a post-doping strategy, most of the dopant atoms are expected to remain in the outer few layers of the CNOs.
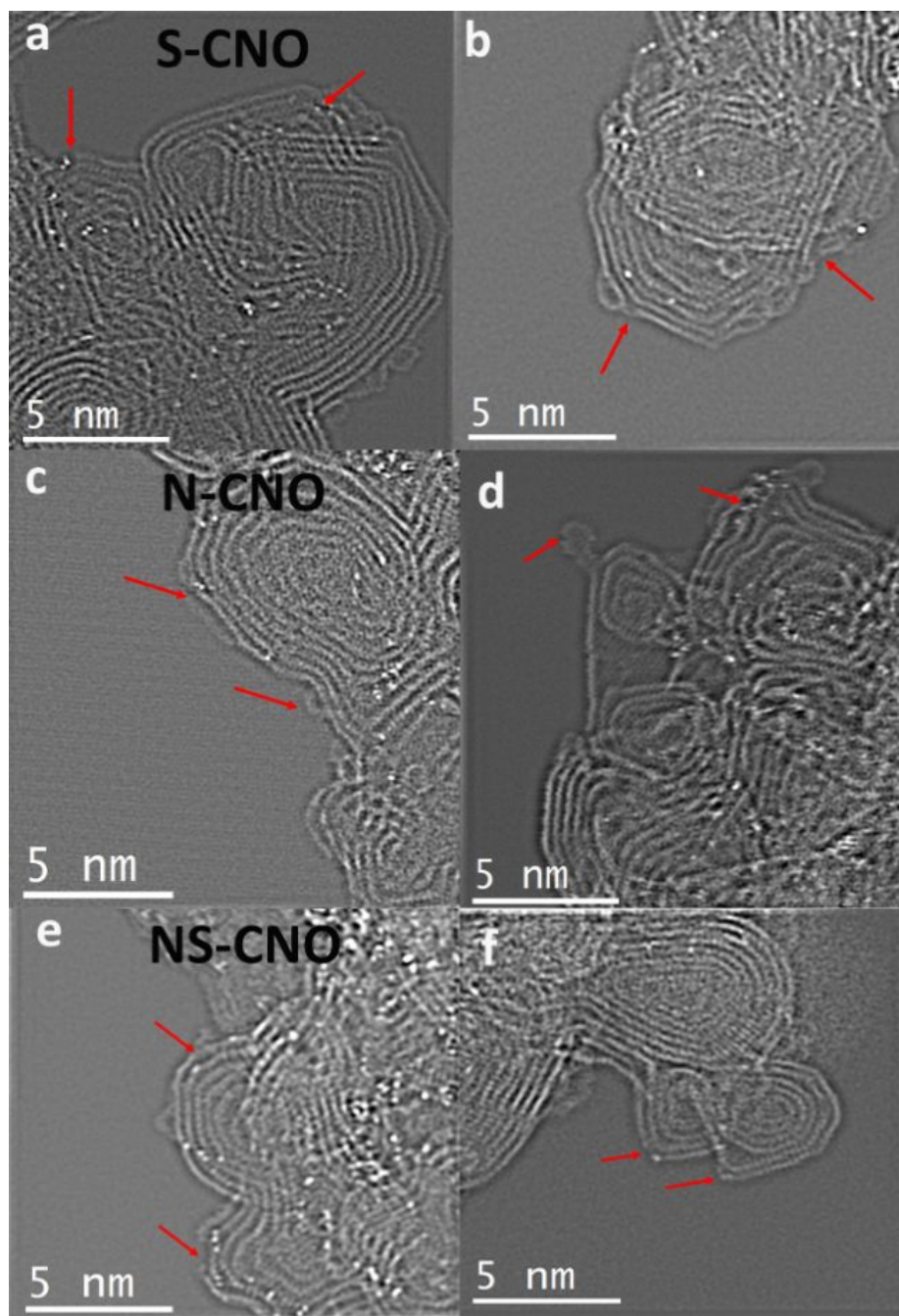
Figure 3. Filtered IFFT images showing defects in CNO shells. (a,b) sulfur-doped CNOs, (c,d) nitrogen-doped CNOs, and (e,f) sulfur and nitrogen co-doped CNOs. (Defects marked with red arrows.)

It was also not possible to distinguish quantitatively whether any particular dopant atom was sulfur or nitrogen (or possibly oxygen) in the co-doped sample, due to unknown sample thickness and variation. In all cases dopants were identified qualitatively as atoms with greater intensity (and therefore mass) than carbon. A control experiment was performed to confirm that the undoped pristine CNO starting material does not contain visible heteroatom dopants. The HAADF micrographs and corresponding filtered images (Fig. S5) show samples free of contaminants, and demonstrate that the heteroatoms observed in Fig. 3 likely originate from S and/or N doping. Consistent with HAADF imaging, dopants in the S-CNO and NS-CNO samples were more easily identified due to their greater intensity (Fig. S6). The results show that for NS-CNO, 86% of dopant atoms are located within <0.4 nm of the defect site, whereas for S-CNO and N-CNO, only 57% and 28% of dopant atoms reside within <0.4 nm of the defect site respectively (Fig. 4a and Fig. S7 (detailed

histogram of Fig. 4a with equal bin sizes)). While most of the dopants in NS-CNOs and S-CNOs are found at the defect sites or within close proximity to defects, N dopants in N-CNOs are significantly internalized and at longer distances from defects, where the dopants are presumed to be introduced. This is attributable to the smaller size of N with respect to S. The configuration of dopant atoms (whether single or grouped) is consistent throughout the three samples (Table 1; and Fig. 4b). In N-, S-, and NS-CNO samples, the ratios of single to grouped dopant atom configurations are 1:1.4, 1:1.8, and 1:1.4 respectively. Li et al. have reported that the defects are inferred to be located near high curvature locations on CNO and can be seen as blurry areas in TEM/STEM images, which is also consistent with our work.[9] STEM imaging and EELS reveals, therefore, the occurrence of dopant atoms and groups at close proximity to high curvature regions of the shell, in which defects are more prevalent.

Table 1. Dopant configuration and location on CNOs

Type	Number of CNO	Number of dopants	grouped dopant atoms				single atom dopants		Proximity to defect sites							
			2	3	>3	%			At the defect site		0-0.4 nm		0.41-0.7 nm		>0.7 nm	
NS-CNO	39	>209	23	10	3	42	121	58%	147	70%	34	16%	11	5%	17	8%
S-CNO	29	>82	7	3	1	32	55	67%	43	52%	4	5%	13	16%	22	27%
N-CNO	30	>67	8	4	-	42	39	58%	16	24%	3	4%	5	7%	43	64%
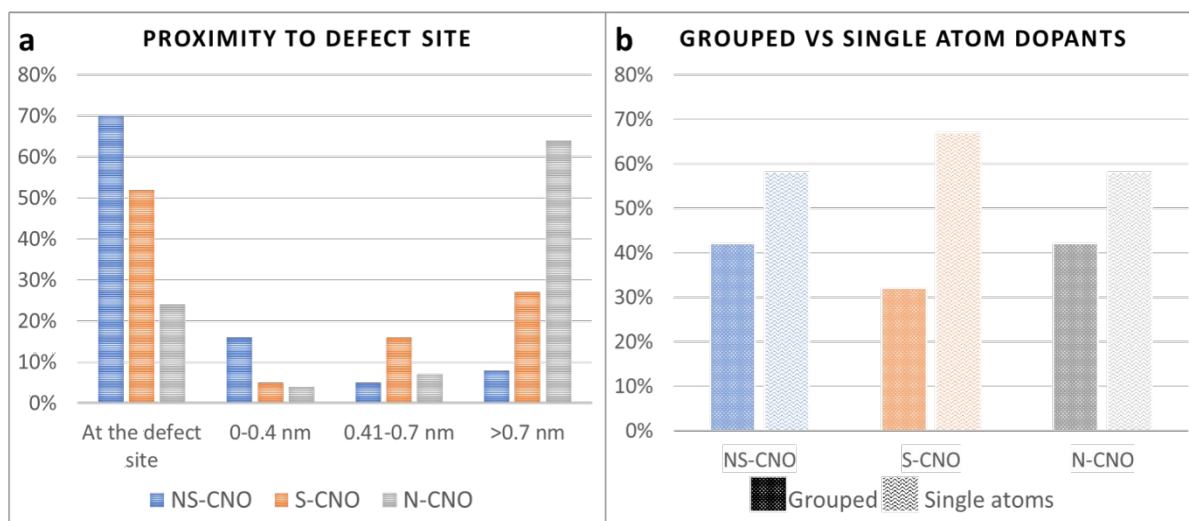
Figure 4. Histograms of dopant proximity and configuration in the three CNO samples. (a) Proximity of defect sites, and (b) single atom vs grouped configuration. The bin sizes in (a) were chosen to best illustrate the trend in dopant's proximity to defect site.

Since all samples studied show distinct atomic configurations and distributions, the electronic properties of these samples might also be expected to be significantly different from one another. Accordingly, the ORR electrocatalytic activities of these samples were measured as a metric to differentiate the electronic properties. The ORR is one of the crucial reactions to occur in fuel cells and metal air batteries.[26] Typically, the oxygen reduction occurring in the cathode side of a fuel cell is kinetically sluggish and more problematic compared to hydrogen oxidation occurring at the anode. It is imperative, therefore, to boost the kinetics of the ORR by developing advanced materials which are highly stable and durable. In an alkaline medium, the ORR proceeds either by a direct four-electron pathway or a two-electron peroxide pathway.[27]

Direct four-electron pathway
$O_2 + 2H_2O + 4e^- \rightarrow 4OH^-$ = 0.401 V vs. SHE

Two-electron peroxide pathway
$O_2 + H_2O + 2e^- \rightarrow HO_2^- + OH^-$ = -0.065 V vs. SHE
$HO_2^- + H_2O + 2e^- \rightarrow 3OH^-$ = 0.867 V vs. RHE
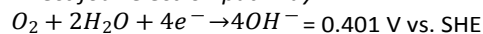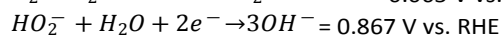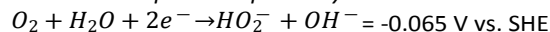
Out of these two pathways, the direct four-electron pathway is desirable due to its high efficiency. It has been proposed that heteroatom dopant atoms such as sulfur and nitrogen incorporated into a graphitic network are effective in inducing asymmetric charge distribution on the surface due to dissimilar electronegativity and size mismatch.[3,14,28] The greater electronegativity difference between nitrogen and carbon induce an asymmetric charge density; the size mismatch between carbon and sulfur also yield an asymmetric charge density. Co-doped nitrogen and sulfur introduce unpaired electrons altering the charge and spin densities of the active domains. Sites with high spin and charge densities are known to active for the adsorption of oxygen molecule during the ORR.[9,15] Figure 5a shows LSV recorded for each catalyst sample. The ORR performance of each tested catalyst was compared with the state-of-the-art 20% Pt-C catalyst, where the best ORR catalyst shows low-overpotential and a high current density. Figure 5b compares the onset potential and the current densities at -0.50 V vs. Ag/AgCl of each catalyst. It is noted that, out of all the metal-free catalysts investigated, NS-CNO show the lowest on-set potential and the highest current density (with current density similar to that of Pt-C). N-CNO sample showed higher performance than S-CNO sample. Undoped CNOs showed the worst performance. Intriguingly, all heteroatom-doped samples yielded electron transfer numbers close to four indicating the heteroatom dopant contribution towards ORR. Since undoped CNOs do not contain heteroatoms, this material primarily generates peroxide via a two-electron pathway. The narrow four-electron window of undoped CNOs (-0.1 V - 0.0 V) is a mathematical artifact due to a near-zero ring current (I_r). These observations are well consistent with the other literature findings.[29]
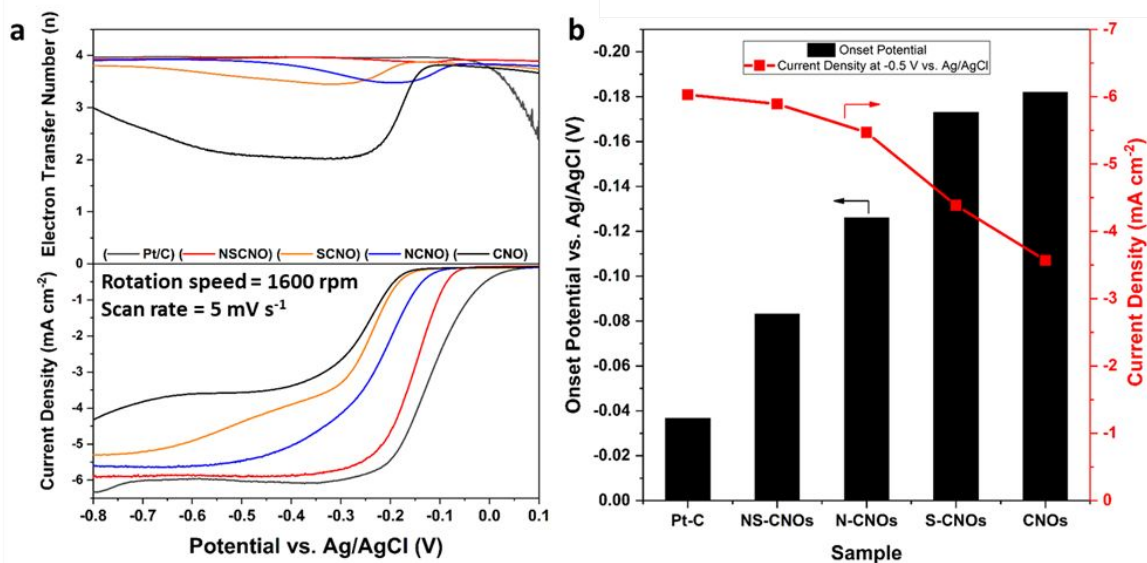
Figure 5. Determination of ORR activity by RRDE experiments. (a) LSV curves and electron transfer number (obtained by rotating RRDE at 1600 rpm while maintaining a scan rate of 5 mV s^{-1}) and (b) Current density and ORR onset potential for each sample.

ARTICLE

Overall, all heteroatom-doped CNOs exhibit enhanced activities for the ORR compared to undoped CNOs, in terms of higher current densities and lower onset potentials. Among doped CNOs, NS-CNOs show the best performances that are close to Pt/C. Remarkable improvements in the activities of doped CNOs clearly reflect that various active sites are formed by incorporating S and N dopants in CNOs. From STEM analysis, N-CNO, S-CNO, and NS-CNO contain dopants in the form of groups at or closer to defect sites. These groups could form unique active sites that can reduce the adsorption barrier of O_2 molecule and catalyze ORR. Previous computational studies identified bi- and tri- pyridinic N sites as potential catalytic sites.[30,31] These sites can have dopant arrangements as groups that we captured by STEM analysis in this study. In NS-CNO where N and S atoms are in proximity, in particular, the electron and spin densities on the catalyst surface are significantly promoted relative to N-CNO or S-CNO, leading to the best ORR activity. Combined with the structural analysis presented, NS-CNO suggests a concerted mechanism of catalysis for the ORR, requiring both heteroatom dopant and high-curvature defective regions of the CNO.

Conclusions

In this work, for the first time, single and grouped dopant atoms in S-, N- and NS-CNO samples were resolved using STEM imaging. Micrographs show that the onion like concentric shell structure of the CNO was retained during the fabrication and doping steps, and EELS characterization confirms the successful doping of all three CNO samples. Defects within CNO shells are seen clearly in HRSTEM images and analysis shows that 86% of dopant atoms in the NS-CNO sample are located within <0.4 nm of the defect, while the dopant atoms in S- and N-CNO are located at greater distances from the defects, revealing a possible key structural feature for catalysis. Greater catalytic efficiency for the ORR for co-doped samples with respect to singly-doped counterparts suggests the synergistic effect of dopants and the dopant proximity to the defect may play a key role in the catalytic mechanism.

Conflicts of interest

There are no conflicts to declare.

Acknowledgements

Notes and references

#these two authors contributed equally.
*Corresponding authors:
beth.guiton@uky.edu, dooyoung.kim@uky.edu

Author Contributions

M.P.T designed and conducted the STEM experiments and characterization under the guidance of B.S.G., with contribution from M.D.A.G. N.W. synthesized CNO samples and conducted catalysis experiments under the guidance of D.Y.K. Both B.S.G. and D.Y.K. guided the research and experimental design. The manuscript was written through contributions of all authors. All authors have given approval to the final version of the manuscript.

1   C. Han, X. Bo, Y. Zhang, M. Li and L. Guo, *Journal of Power Sources*, 2014, **272**, 267–276.
2   O. Mykhailiv, K. Brzezinski, B. Sulikowski, Z. Olejniczak, M. Gras, G. Lota, A. Molina-Ontoria, M. Jakubczyk, L. Echegoyen and M. E. Plonska-Brzezinska, *Chemistry – A European Journal*, 2017, **23**, 7132–7141.
3   J. P. Paraknowitsch and A. Thomas, *Energy Environ. Sci.*, 2013, **6**, 2839–2855.
4   E. Y. Choi and C. K. Kim, *Scientific Reports*, 2017, **7**, 4178.
5   L. Yang, S. Jiang, Y. Zhao, L. Zhu, S. Chen, X. Wang, Q. Wu, J. Ma, Y. Ma and Z. Hu, *Angewandte Chemie International Edition*, 2011, **50**, 7132–7135.
6   Y.-C. Lin, P.-Y. Teng, C.-H. Yeh, M. Koshino, P.-W. Chiu and K. Suenaga, *Nano Lett.*, 2015, **15**, 7408–7413.
7   G. Wu, N. H. Mack, W. Gao, S. Ma, R. Zhong, J. Han, J. K. Baldwin and P. Zelenay, *ACS Nano*, 2012, **6**, 9764–9776.
8   Y. Lin, X. Pan, W. Qi, B. Zhang and D. Sheng Su, *Journal of Materials Chemistry A*, 2014, **2**, 12475–12483.
9   M. Li, W. Liu, H. Zhang, Z. Liang, P. Duan, X. Yan, P. Guan, B. Xu and J. Guo, *Physical Chemistry Chemical Physics*, 2018, **20**, 2022–2027.
10   Y. Liu and D. Y. Kim, *Electrochimica Acta*, 2014, **139**, 82–87.
11   T. Oku, G. Schmid and K. Suganuma, *J. Mater. Chem.*, 1998, **8**, 2113–2117.
12   D. Xiong, X. Li, L. Fan and Z. Bai, *Catalysts*, 2018, **8**, 301.
13   X.-F. Yang, A. Wang, B. Qiao, J. Li, J. Liu and T. Zhang, *Acc. Chem. Res.*, 2013, **46**, 1740–1748.
14   J. Liang, Y. Jiao, M. Jaroniec and S. Z. Qiao, *Angewandte Chemie International Edition*, 2012, **51**, 11496–11500.
15   Z. Wu, M. Song, J. Wang and X. Liu, *Catalysts*, 2018, **8**, 196.
16   A. Palkar, F. Melin, C. M. Cardona, B. Elliott, A. K. Naskar, D. D. Edie, A. Kumbhar and L. Echegoyen, *Chemistry – An Asian Journal*, 2007, **2**, 625–633.
17   C. Tang and Q. Zhang, *Advanced Materials*, 2017, **29**, 1604103.
18   G. Wu, M. Nelson, S. Ma, H. Meng, G. Cui and P. K. Shen, *Carbon*, 2011, **49**, 3972–3982.
19   N. Wanninayake, Q. Ai, R. Zhou, M. A. Hoque, S. Herrell, M. I. Guzman, C. Risko and D. Y. Kim, *Carbon*, 2020, **157**, 408–419.
20   N. Wanninayake, A. Qianxiang, M. Thomas, U. S. Kodithuwakku, A. Hoque, M. I. Guzman, B. Guiton, C. Risko and D. Y. Kim, *Meet. Abstr.*, 2019, **MA2019-01**, 1591–1591.
21   S. Iijima, *Journal of Crystal Growth*, 1980, **50**, 675–683.
22   V. L. Kuznetsov, A. L. Chuvilin, Y. V. Butenko, I. Yu. Mal'kov and V. M. Titov, *Chemical Physics Letters*, 1994, **222**, 343–348.

23   J. A. Hachtel, J. C. Idrobo and M. Chi, *Advanced Structural and Chemical Imaging*, 2018, **4**, 10.

24   Z. W. Wang, Z. Y. Li, S. J. Park, A. Abdela, D. Tang and R. E. Palmer, *Phys. Rev. B*, 2011, **84**, 073408.

25   L. G. Cançado, A. Jorio, E. H. M. Ferreira, F. Stavale, C. A. Achete, R. B. Capaz, M. V. O. Moutinho, A. Lombardo, T. S. Kulmala and A. C. Ferrari, *Nano Lett.*, 2011, **11**, 3190–3196.

26   R. Ma, G. Lin, Y. Zhou, Q. Liu, T. Zhang, G. Shan, M. Yang and J. Wang, *npj Comput Mater*, 2019, **5**, 1–15.

27   B. Šljukić, C. E. Banks and R. G. Compton, *Journal of the Iranian Chemical Society*, 2005, **2**, 1–25.

28   J.-F. Chen, Y. Mao, H.-F. Wang and P. Hu, *ACS Catal.*, 2016, **6**, 6804–6813.

29   N. Ramaswamy and S. Mukerjee, *Advances in Physical Chemistry*, 2012, **2012**, 1–17.

30   J. Zhang, Z. Xia and L. Dai, *Science Advances*, 2015, **1**, e1500564.

31   H. Deng, Q. Li, J. Liu and F. Wang, *Carbon*, 2017, **112**, 219–229.

Direct visualization of dopant atom configuration in carbon nano-onions provides structure-property link to catalytic activity